J. Fluid Mech. (1972), *vol.* 53, *part* 1, *pp.* 17–44
Printed in Great Britain

The excitation of resonant triads by single internal waves

By SEELYE MARTIN,
University of Washington, Seattle
WILLIAM SIMMONS
Woods Hole Oceanographic Institution
AND CARL WUNSCH
Massachusetts Institute of Technology

(Received 9 August 1971)

The stability of progressive internal waves of modes 1 and 3, propagating down a long tank filled with a linearly stratified salt water solution, is studied theoretically and experimentally. Examination of the spectra of the waves shows when $al > 10^{-2}$, where a is the wave amplitude and l is the vertical wavenumber, that single internal waves excite waves of several resonant triads, where the excited waves belong to that set of triads with the largest theoretical growth rates. For example, a wave of mode 3 with a non-dimensional frequency around 0·66 excites waves of the following triads: (5, 8, 3), (6, 9, 3), (8, 11, 3), (9, 12, 3) and (10, 13, 3), where the integers are mode numbers. The spontaneous appearance of these naturally excited triads greatly complicates attempts to isolate and study preselected wave interactions. In one case, when waves of mode 1 and 3 with $al > 10^{-2}$ were generated simultaneously while tuned to the (1, 3, 4, 7) multiple resonance, the fastest growing wave was neither a wave of mode 4 located at the difference frequency nor a wave of mode 7 at the sum frequency, but rather a wave of mode 9 located at a frequency slightly above that of the 4-wave.

1. Introduction

Davis & Acrivos (1967) first demonstrated the importance of nonlinear resonant interactions in inducing internal wave instabilities. They investigated the propagation of internal waves in a fluid consisting of two homogeneous layers separated by a strongly stratified layer of thickness 1 cm. They discovered that as a large amplitude 1-wave† propagates down the channel, a 2-wave, which has a frequency distinct from that of the 1-wave and its harmonics, appears and distorts the 1-wave. Their measurements suggest that the 1-wave broke up into a (1, 2, 3) resonant triad, with the 1- and 2-waves propagating downstream, and the 3-wave propagating upstream. In their analysis of the experiment, however, they did not explain why other similar triads, such as the (1, 3, 2), with the 1- and 3-waves directed upstream and the 2-wave directed downstream, did not appear

† For the sake of brevity, we call a wave of mode 1 a 1-wave; a wave of mode 2, a 2-wave; and so forth. We also call the resonant triad which is made up of, e.g., a 1-wave, a 2-wave and a 3-wave a (1, 2, 3) triad.

in their tank. Further, their relatively small tank and correspondingly high rate of viscous dissipation filtered out other possible unstable triads made up of high mode number waves. Still, their work both clearly demonstrated that internal waves are unstable, and provided good evidence of the resonance mechanism.

Martin, Simmons & Wunsch (1969) studied the resonant interaction between two internal waves of very small steepness in a linearly stratified fluid of depth 1 m. Their experiment showed that, if a small 1-wave and a small 3-wave were generated, but at levels well below those required to induce the resonant instability discussed herein, and tuned to a (1, 3, 4) resonant triad with the 1- and 3-wave propagating downstream, then a 4-wave with the predicted frequency and wavelength and with amplitude of the same order as the generated waves does in fact appear and propagates upstream. The experiment also brought out the existence of 'multiple' resonances, i.e. tunings for which the 3- and 4-waves of a particular (1, 3, 4) resonant triad are also members of a (3, 4, 7) triad.

In the present investigation, using the same apparatus as Martin, Simmons & Wunsch, we explore the wave fields induced by generating one or two moderately large amplitude waves of fixed frequency.† Because viscous effects are small, such waves can in principle spontaneously produce many other waves at different frequencies and mode numbers. We therefore designed an experiment to determine the modal structure of these other waves over a limited frequency range for the 1- and 3-waves. Within that range, we conclusively identify the other peaks as members of resonant triads associated with the paddle-generated waves. The large number of triads excited by a single wave (we positively identified members of 4 and sometimes 5 triads for the 3-wave and 1 or 2 for the 1-wave) shows that resonant interactions provide a powerful mechanism for transferring energy from a single driving frequency to other parts of the spectrum, and therein lies their geophysical interest.

In § 2 we describe our experimental apparatus, and in § 3 we provide some of the theoretical basis for the work. Finally, § 4 contains the presentation and discussion of the experimental results.

2. The apparatus

The apparatus consisted of a long channel filled with a linearly stratified fluid through which internal waves propagated (figure 1). At one end of the tank, a paddle generated internal waves, which propagated to the other end, where they were absorbed by a beach. At various locations in the tank, we used conductivity sensors to measure the wave amplitudes. The tank is 1·2 m wide, 1·2 m deep, and 21 m long. Glass panels line one wall of the tank, and a variable-speed tow carriage runs over the tank.

To fill the tank with a linearly stratified fluid, we followed the method of Clark, Stockhausen & Kennedy (1967). We measured the density profile by withdrawing samples from the fluid at 10 cm intervals in the vertical, then weighing them on a specific gravity balance. The density gradient was nearly linear with a mean Brunt

† McEwan (1971) does a similar experimental and theoretical study of the stability of standing internal waves.

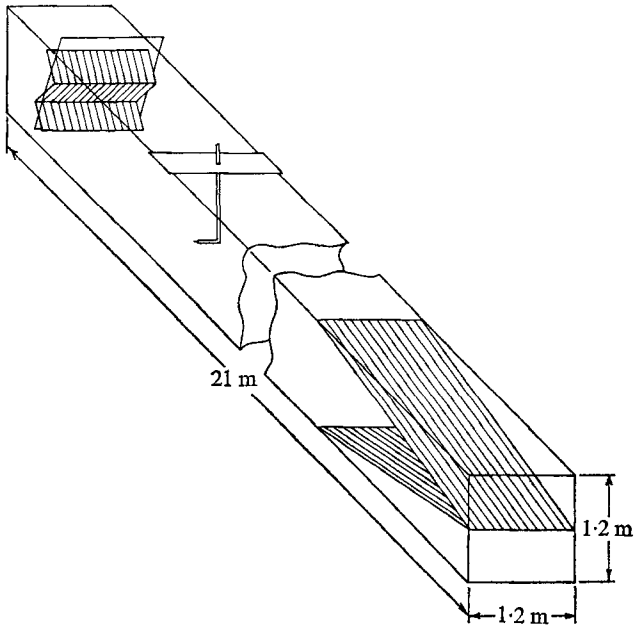

FIGURE 1. A schematic, perspective view of the wave tank, paddle, beach, and of a typical conductivity probe.

frequency of about 0·42 radians $\sec^{-1}$ (see e.g. Martin, Simmons & Wunsch). This stratification persisted with very little change for at least 14 days, after which time homogeneous layers of a thickness of about 10 cm at the top and bottom became apparent.

To excite waves of modes 1 and 3, we designed the paddle to consist of two parts (figure 2). First, a d.c. motor, through a simple eccentric linkage, oscillated a large frame in periodic motion about a pivot located 50 cm above the bottom of the tank. Three smaller paddles, of dimensions 1 m by 33·3 cm, were mounted on the large frame. When we fixed these paddles in the same plane, the periodic motion of the large frame primarily generated a wave of mode 1. The amplitude of the next largest wave generated by the large frame has mode 3 and is $\frac{1}{9}$ the amplitude of the wave of mode 1 (see Thorpe 1968). The half-angle displacement α_1 of the large frame could be varied in 0·5° steps from 1° to 5°.

The three smaller paddles pivoted about points 16·7 cm, 50 cm, and 83·4 cm above the bottom of the tank. A second motor mounted on the large frame oscillated these paddles. A slot-and-pin linkage drove the middle paddle 180° out-of-phase with the upper and lower paddles, thereby primarily generating a wave of mode 3. The half-angle displacement α_3 of the smaller paddles could be varied in 1° steps from 4° to 9°. Simultaneous operation of the two motors allowed us to superimpose each mode linearly.

From Thorpe (1968, p. 603), the theoretical amplitude a_n of the wave generated by the paddle as a function of the half-angle displacement α_n is

$$a_n = \frac{8H_n D\kappa \sin \alpha_n}{n\pi^3}, \tag{2.1}$$

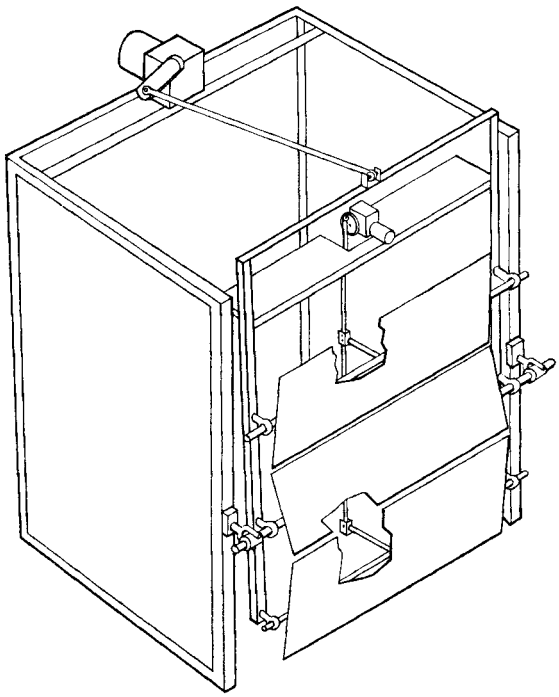

FIGURE 2. A detailed drawing of the paddle.

where $n = 1$ or 3 is the mode number; H_n is half the height of a paddle blade for the particular mode where $H_1 = 50$ cm and $H_3 = 16{\cdot}7$ cm; D is the fluid depth; and κ is the wavenumber of the generated wave. Because of both viscous dissipation and the resonant interactions, the observed wave amplitudes fell below that predicted by (2.1).

To prevent sloshing around the edges of the paddles, we taped thin sheets of neoprene rubber from the edges of the paddles to the sides of the tank. Rubber flaps also covered the horizontal openings between the paddles. To damp out waves in the space behind the paddle, we filled this space with a stack of loose packing hair. A simple transducer which was mounted on the tank and attached to the uppermost of the three paddles gave a voltage output which was proportional to the paddle displacement. Observations with dye showed that away from the immediate vicinity of the paddle, where the shear between the edges of the paddle and the side walls of the tank generated vortices which rotated with the period of the wave, the waves were two-dimensional.

At the other end of the tank, about 17 m downstream of the paddle, a wedge-shaped beach (figure 1) absorbed the incident waves. Wunsch (1969) shows that if β is the half-angle of the beach then waves of frequency

$$\omega/N \geqslant \sin\beta \tag{2.2}$$

are totally absorbed; while waves of frequency

$$\omega/N < \sin\beta$$

are totally reflected. For our wedge, $\beta = 11{\cdot}5°$, so that $\sin\beta = 0{\cdot}2$. The non-

dimensional frequencies of the waves which were generated in the experiments, both by the paddle and by resonant interactions, were above this frequency. The planes of the wedge were made from marine plywood; to increase viscous damping, the lower plane was lined with a 5 cm thick sheet of packing hair.

Observations made on the flow in the beach showed that there were no observable reflexions of the waves which satisfied the inequality (2.2). Not all of the wave energy, however, was absorbed by viscosity; we observed, particularly for mode 1, that some wave-breaking occurred in the beach. The mixing generated by this breaking had no observable effect on the density profile.

To record the internal waves, we used arrays of single-electrode conductivity probes which detected vertical displacements of order 5×10^{-2} cm. Appendix A gives details on the design and use of these probes. As is shown there, the nonlinearities which arise directly from the probe circuitry amount to about 0.1 %. In the experiment, a much greater source of nonlinearity came from the curvature of the density gradient. We estimate the size of this term at 1 % for a 5 cm displacement. For a wave at a single frequency, the effect of this nonlinearity is to generate spurious harmonics: for waves at two different frequencies, the nonlinearities generate peaks at the sum and difference frequencies as well as spurious harmonics. One can easily show that in our case the amplitudes of the spurious peaks are less than 1 % of the amplitudes of the generated waves.

We calibrated the probes in the tank, by displacing them a known distance in the vertical above and below their equilibrium positions. The rectified output of the circuitry was adjusted to yield approximately 1 volt cm^{-1}. During an experiment, we used a digital recorder which sampled the entire probe array and the paddle-mounted transducer once every 2 sec. Then, using standard techniques, the data were listed and Fourier-analysed. We computed the dispersion relations for the various modes and frequency ranges of interest from the measured gradient using a computer program developed by Perkins (1970).

3. Kinematics and dynamics of resonant instabilities

The results of both the analytical methods of perturbation theory and two-scale averaging applied to the Boussinesq equations of motion, subject to the constraints imposed by the second-order kinematic resonance conditions, are by now familiar to most workers with an interest in wave theories. This section assumes familiarity with those results. A derivation for the internal waves considered here is included in appendix B.

In any second-order resonant triad, the wave of maximum frequency, in absolute value, is unstable to wave perturbations at the other two frequencies, as was derived by Hasselmann (1967). Thus, e.g. a 3-wave is unstable in all $(3, n, n+3)$ triads for which $|\omega_3| > |\omega_n|$ and $|\omega_3| > |\omega_{n+3}|$, following in the sense. First, $a_3 = \text{constant}$, $a_n = a_{n+3} = 0$ is a solution of the interaction equations (e.g. (3.1), which neglect slow spatial variations). If it is noted both that (i) the three interaction coefficients $E_{i,j}$, $j = 1, 2, 3$, of any resonant triad may be written† $\omega_{i,j}\mathscr{E}$, where $\omega_{i,j}$ is wave frequency and $\mathscr{E}$ depends upon the wave

† This representation renders the proofs of the conservation theorems in appendix B trivial.

parameters for the particular triad (Hasselmann 1967); and (ii), by the first of (B 13), $\omega_3 < 0$ requires $\omega_n > 0$, and $\omega_{n+3} > 0$, so the interaction equation (B 15) may be written as

$$\left.\begin{aligned} \partial a_3/\partial T &= -|\omega_3|\,\mathscr{E} a_n a_{n+3}, \\ \partial a_n/\partial T &= |\omega_n|\,\mathscr{E} a_{n+3} a_3, \\ \partial a_{n+3}/\partial T &= |\omega_{n+3}|\,\mathscr{E} a_3 a_n. \end{aligned}\right\} \tag{3.1}$$

From (3.1) it may easily be shown that arbitrarily small wave perturbations from the n and $n+3$ resonant partners will grow, drawing energy from the 3-wave. The initial growth of these perturbations is of the form

$$\left.\begin{aligned} a_n &= \overline{a_n} \exp\{\overline{a_3}\mathscr{E}(\omega_n \omega_{n+3})^{\frac{1}{2}} t\}, \\ a_{n+3} &= \overline{a_{n+3}} \exp\{\overline{a_3}\mathscr{E}(\omega_n \omega_{n+3})^{\frac{1}{2}} t\}. \end{aligned}\right\} \tag{3.2}$$

Thus, according to this linearized instability theory, the amplitude of a perturbation at any time is determined by both (i) its growth rate, which is the product of (*a*) a purely kinematic quantity, e.g. $\mathscr{E}(\omega_n \omega_{n+3})^{\frac{1}{2}}$, and (*b*) the initial amplitude $\overline{a_3}$ of the unstable wave, and (ii) the initial amplitude $\overline{a_n}$ or $\overline{a_{n+3}}$ of the perturbation. In our tank, the perturbations are caused by background noise.

The resonant interaction equations for a single triad of waves result from a *nonlinear* dynamical system, rendering superposition a seemingly unlikely procedure. But in fact, Fourier decomposition allows the superposition of interaction equations for whole sets of triads having one wave in common, e.g. (3, 3, 6), (3, 4, 7), (3, 5, 8), etc. This superposition is also possible for pairs of triads having two waves in common, such as the (1, 3, 4) and (3, 4, 7), which make up the (1, 3, 4, 7) multiple quartet† to be described in § 4.4. In both cases, superposition leads to a physically sensible theory with regard to conservation theorems (appendix B) and interaction equations which possess the elementary solutions $a_3 =$ constant, $a_i = 0$ for $i \neq 3$, the stabilities of which are investigated herein. The linearized instability calculation which, for a single triad, yields (3.2), may be performed on the set of triads mentioned above, and leads to the conclusion that unstable perturbations from any one triad grow independently of the perturbations from any other triad.

By contrast, the instability calculation applied to either of the two common waves of the two triads constituting a multiple quartet gives the square of the perturbation growth rate as the sum of the squares of the growth rates from each of the individual triad interactions. Now, the 3-wave of the (1, 3, 4, 7) multiple tuning is unstable in the (3, 4, 7) triad (i.e. $(E_4 E_7)_{(3,4,7)}$ is positive), but stable in the (1, 3, 4) triad (i.e. $(E_1 E_4)_{(1,3,4)}$ is negative). Thus, the stability of a 3-wave at the (1, 3, 4, 7) tuning is determined by the sign of $(E_4 E_7)_{(3,4,7)} + (E_1 E_4)_{(1,3,4)}$. For the (1, 3, 4, 7) studied experimentally here, this sum is positive, and, since $(E_1 E_4)_{(1,3,4)} \cong -\frac{1}{2}(E_4 E_7)_{(3,4,7)}$, the net effects of the multiple tuning on the stability of the 3-wave are (i) to reduce the growth rate of the 4-, and 7-perturbations by about $\sqrt{\frac{1}{2}}$, and (ii) to allow the growth of a 1-wave, whose frequency is *greater* than $|\omega_3|$, at the same rate. The 4-wave of the (1, 3, 4, 7) quartet is stable in both the (1, 3, 4) and (3, 4, 7) triads. Hence, it is stable at the multiple tuning.

† All multiple interaction quartets are formed of pairs of triads having two waves in common.

The stabilities of the 1- and 7-waves at this tuning are unaffected by the multiple interaction and they behave, to lowest order, as they would in their individual triads.

In our experiments, we studied the 3-wave of frequency $\omega/N = 0{\cdot}66$. A numerical search for triads, and exploration of the kinematic part of their growth rates, reveals that the 3-wave near $\omega/N = 0{\cdot}66$ is unstable to wave perturbations from either of two singly infinite sets of resonant triads. These, which we call set I and II, have the modal form $(3, n, n+3)$, $n = 1, 2, 3, \ldots$. For $|n| \geqslant 4$, set I has mode 3 and $n+3$ travelling away from the paddle and mode n toward it, whereas set II has mode 3 and n travelling away from the paddle and mode $n+3$ towards it. For $|n| \leqslant 3$, the rules for directions of propagation and growth rates are irregular. But all of the growth rates for $|n| \leqslant 3$ are small, with the exception of the $(3, 2, 5)$ at $\omega_3/N \sim 0{\cdot}65$, $\omega_2/N \sim 0{\cdot}28$ and $\omega_5/N \sim 0{\cdot}37$. The growth rates of this $(3, 2, 5)$ and of *all* the members of set I with $|n| \geqslant 4$ are the largest theoretical growth rates with nearly constant computed values of about

$$\overline{a_3}\sqrt{12\,\pi N/10D}.$$

For $|n| \geqslant 4$ the growth rates in both sets I and II increase very slowly and monotonically with n, but with finite limits. As $n \to \infty$, ω_n and $\omega_{n+3} \to \frac{1}{2}\omega_3$, so $E_n \to E_{n+3}$, and for set I

$$\lim_{n\to\infty} E_n/\omega_n = (3\pi N/D)\,[A(1+\omega_3^2/2) + \tfrac{1}{2}(1-\omega_3^2) - (1-\omega_3^2/4)/2A],$$

where $A = [(1-\omega_3^2/4)/(1-\omega_3^2)]^{\frac{1}{2}}$. Section 4 shows that members of set I, which have the largest computed growth rates, are the waves observed in the breakdown of the unstable 3-wave.

Set II has properties similar to set I. As $n \to \infty$, ω_n and $\omega_{n+3} \to \frac{1}{2}\omega_3$, and the limiting form of E_n is similar to the form calculated for set I. The major difference between the two sets is that the growth rate for a particular triad from set II is less than $\frac{1}{2}$ the growth rate of the corresponding triad from set I. Self-excited peaks from set II would therefore be expected only in experiments of very long duration. Since it is amplitude that determines whether or not a wave component can be detected by a salinity probe, the value of $\overline{a_n}$ or $\overline{a_{n+3}}$ is significant for any relatively short duration experiment. Thus, for example, if there were a higher level of odd than even mode number noise in an experimental wave tank, one would expect to detect odd mode numbered waves drawing energy from an unstable wave long before even modes become detectable.

A similar numerical exploration of growth rates shows that a 1-wave of frequency $\omega_1/N \sim 0{\cdot}88$ is unstable to wave perturbations from either of two sets of resonant triads with the modal form $(1, n, n+1)$, $n = 1, 2, 3, \ldots$, and is most unstable to triads from set I having modes 1 and $n+1$ travelling away from the paddle, and mode n towards it. The kinematic part of the growth rates is typically $\pi\sqrt{6\,N/10D}$ and is about 30 % lower than the corresponding 3-wave range. The growth rates for triads from set II, having mode 1 and n travelling away from the paddle, and mode $n+1$ toward it are smaller, but only by as little as 0·9. In each set, there is a corresponding finite limit for E_n as $n \to \infty$. Thus, all possible wave perturbations for an unstable 1-wave grow at about the same rate, and that

rate is notably smaller than the corresponding rate for a 3-wave. For experiments of the same duration involving 1- and 3-waves of equal non-dimensional amplitudes, we would expect to see fewer peaks from the noise spectrum amplified to the level of detectability for the 1-wave.

Frictional effects both in the body of the fluid and in the boundary layers tend to force the decay of waves, while nonlinear effects tend to induce growth. If the effects of friction from rigid side, top and bottom walls (an overestimation since the upper surface is free in the experiments) and the interior are computed and included in the analysis (by adding a term proportional to $a_{i,j}$ (Phillips 1966, § 3.4) to the right side of (B 15)), one finds that the criterion for, and the rate of, unstable growth are essentially unchanged for waves of mode number less than about 20 (for parameters based on the large, square cross-sectional area of our experimental apparatus). Hence, for these modes, frictional dissipation can be ignored in the parameter ranges covered in these experiments.

For instabilities in the temporal domain, all resonant components with group velocities directed towards the paddle will interact and grow as they approach the paddle, and then reflect from it. To lowest order, the reflexion is linear. However, the reflected wave is passive toward further interaction, since its reversed wavenumber vector fails to satisfy the resonance conditions (B 13). Eventually, then, a standing wave field at the paddle, with a combined standing wave field plus downstream progressive wave, is expected away from the paddle. Although growing waves with group velocities toward the paddle were detected in the experiments (modes 9 and 5 of the 3-wave experiment), we observed no evidence of standing waves.

4. The experimental results

In this section, we discuss three experimental studies of wave stability: § 4.2 discusses the waves generated by the unstable 3-wave; § 4.3, those generated by the unstable 1-wave and § 4.4 discusses the multiple resonance. In § 4.1 we describe the probe array used in the study of the 1- and 3-waves.

4.1. *The dense vertical array*

To resolve the modal structure of the waves generated by the unstable 1- and 3-waves at a distance of 3·46 m from the paddle, we placed 5 probes at depths of 12, 17, 25, 37 and 50 cm, which covers half the depth of the tank; and, at 2·72 m from the paddle, we placed two more probes at depths of 12 and 50 cm. Figure 3 shows how the 3·46 m array resolves mode numbers in the range of 5 to 13 for a linear stratification. Note that the vertical array resolves waves with mode numbers up to 13, with the exception of mode 8, without aliasing. By permitting the calculation of horizontal wavenumbers for some of the even modes and all of the odd modes, the two additional probes at 2·72 m provided a check on the vertical array.

From the time series recorded at each probe, a Fourier transform program listed amplitude and phase versus frequency number. To determine the modal structure associated with a peak in the periodogram, we calculated the amplitudes,

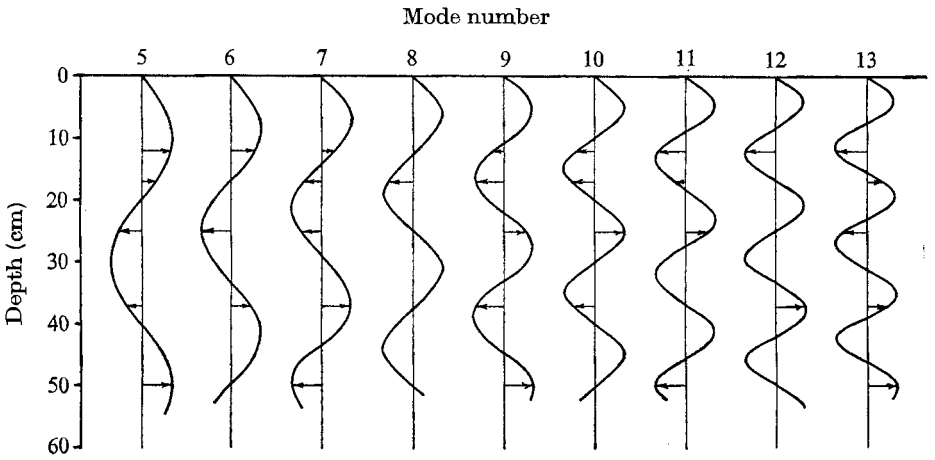

FIGURE 3. Profiles of maximum vertical displacement versus depth in a constant N fluid for modes 5 through 13. The wave amplitudes are arbitrarily set at unity, and the horizontal arrows give the amplitudes at the probe locations.

vertical phase differences and horizontal phase differences for each peak. Except when one of the probes is at a node of a specific mode, wherein the phase difference is arbitrary, the phase difference between any two probes in the vertical array is either $0° \pm \Delta\theta$, or $180° \pm \Delta\theta$. The error term $\Delta\theta$ depends on the signal strength at a given frequency. From the phase difference between two probes separated in the horizontal, we calculate the horizontal wavenumber. If two probes are a distance x_0 apart, and the phase difference at a specific frequency is $\theta_0 \pm \Delta\theta$, then the wavenumber is

$$\kappa = \frac{2n\pi + \theta_0}{x_0} \pm \frac{\Delta\theta}{x_0},$$

where $n = 0, \pm 1, \pm 2, \pm 3, \ldots$.

The resolution of the array is limited by x_0, which must be large enough so that $\Delta\theta/x_0$ is small, but small enough that $2\pi n/x_0$ does not lead to aliasing. In the experiments, $x_0 = 0{\cdot}73$ m and the observed values of $2\pi/\kappa$ ranged from $0{\cdot}35$ m to $1{\cdot}3$ m.

To determine the modal structure, we plotted amplitude versus depth for each spectral peak, using the vertical phase differences to determine the relative signs of the amplitudes, then compared these plots with the modal structure calculated from the measured density gradient to determine the mode number. For the same peak, we also compared the experimentally measured and the theoretically predicted horizontal wavenumber as a check on the mode number determination.

The experiments contain two additional checks on the assignment of mode numbers to given peaks. First, for the experiments involving the 3-wave, the same pattern of peaks and their corresponding mode numbers occurred in several different experiments. Second, as will be seen below, the experimentally measured values of the mode numbers fall either at or very near the frequencies where we would expect them to fall from resonant triad theory.

4.2. *The unstable* 3*-wave*

In this section, we describe the results of two experiments run at the same frequency involving a 3-wave of moderate amplitude. In the first experiment, we generated only the 3-wave; in the second, we added a small 1-wave at a frequency well off resonance. The two experiments were separated in time by 48 h. For both experiments,

$$\omega_3/N = 0{\cdot}654 \quad \text{and} \quad \alpha_3 = 9°,$$

where $N = 0{\cdot}431 \pm 0{\cdot}003\,\text{sec}^{-1}$. The observed density gradient fluctuated very slightly over the period of the experiment. For example, in the first experiment, the theoretical value of κ_3 was $\kappa_3 = 7{\cdot}9\,\text{m}^{-1}$; while, for the second, $\kappa_3 = 8{\cdot}0\,\text{m}^{-1}$. From (2.1), the wave amplitude is $a_3 = 1{\cdot}8$ cm. Thus the horizontal and vertical wave steepnesses for both experiments are very nearly equal at

$$a_3\kappa_3 \simeq a_3 l_3 \simeq 1{\cdot}5\text{–}1{\cdot}7 \times 10^{-1},$$

so that the wave steepnesses are small but finite.

Figure 4, which, for the 3-wave alone case, compares the periodogram of the paddle displacement with that of the signal recorded at a distance of 3·46 m and at a depth of 37 cm, shows that the paddle energy is concentrated at the driving frequency and its harmonics, while the fluid motion has considerable energy at various other frequencies.†

For the same run, figure 5 summarizes the information obtained from the probe array. The lower part of the figure shows the periodogram of the fluid motion at a depth of 50 cm; the upper part, the modal structure associated with each major peak, where the black dots are the measured amplitudes and the dark lines show the calculated modal structure, which is fitted to the observed amplitudes. The numbers in parentheses beside the black dots are the observed phases. In plotting the amplitudes, we interpret phase shifts within $\pm 30°$ of $90°$ to mean that the relative sign of the amplitude is indeterminant. For these cases, an amplitude a at a particular height is plotted as both $\pm a$, as occurs at the 37 cm level of the 13 wave. This phase indeterminacy occurs either when the wave amplitude is very small or when the probe is near the node of a specific mode. The slight nonlinearities in the density gradient increasingly influence the shape of the wave profile for a given wave as both its mode number and frequency increase. This accounts for the deviations from a sinusoidal profile of the 3- and 13-waves in figure 5.

Above the modal structure, for each wave, we list its mode number, the observed frequency ω/N, and the theoretical and measured value of the horizontal wavenumber. If we assume that the accuracy of the measured phase differences in the vertical and horizontal are of the same order, namely 15–30°, then the error $\Delta\kappa$ associated with the horizontal wavenumbers varies between 0·35 to 0·70 m^{-1}. With the exception of the 13-wave, the measured and theoretical value of κ very nearly agree.

† Self-interactions are, in principle, dynamically impossible at second order. Peaks such as the one at $2\omega_3$ on the upper trace can be generated at other orders, although the horizontal and vertical length scales of this wave need not correspond to a second harmonic.

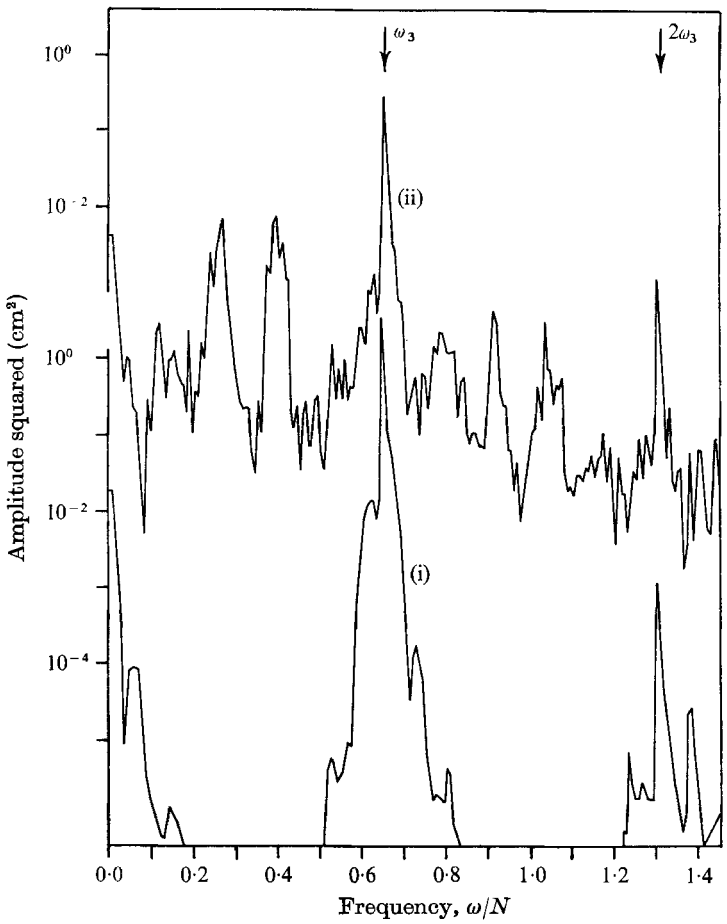

FIGURE 4. Comparison of the periodogram (i) of the paddle displacement for the 3-wave alone ($\alpha = 9°$, $N = 0{\cdot}431\ \mathrm{sec}^{-1}$) with that of (ii) the fluid motion measured at 3·47 m downstream at a depth of 37 cm.

The arrows under the periodogram show the calculated positions of the resonant triads (4, 7, 3) through (10, 13, 3), which are all members of set I (§ 3), associated with the unstable 3-wave. For comparison, figure 5 also shows the location of two possible triads which were not excited; the (2, 1, 3) and the (4, 1, 3). Not shown on figure 5 is the location of the (2, 3, 5) triad, whose growth rate is equal to the triads in set I, and for which all three waves propagate downstream. The calculated position of this triad is $\omega_3/N = 0{\cdot}654$, $\omega_2/N = 0{\cdot}304$, and $\omega_5/N = 0{\cdot}350$. Aside from the sidelobe at $\omega/N = 0{\cdot}350$, which is generated by the adjacent 13-wave peak, there are no wave-generated peaks on figure 5 at the frequencies of the 2- and 5-waves. As an example of one of the excited triads, the following waves make up the (5, 8, 3) triad:†

$$\omega_5/N = 0{\cdot}232, \quad \kappa_5 = -3{\cdot}9\ \mathrm{m}^{-1},$$
$$\omega_8/N = 0{\cdot}422, \quad \kappa_8 = 11{\cdot}8\ \mathrm{m}^{-1},$$
and
$$\omega_3/N = 0{\cdot}654, \quad \kappa_3 = 7{\cdot}9\ \mathrm{m}^{-1}.$$

† For purposes of calculation in (B 13)–(B 18), ω_3/N and κ_3 would have negative signs.

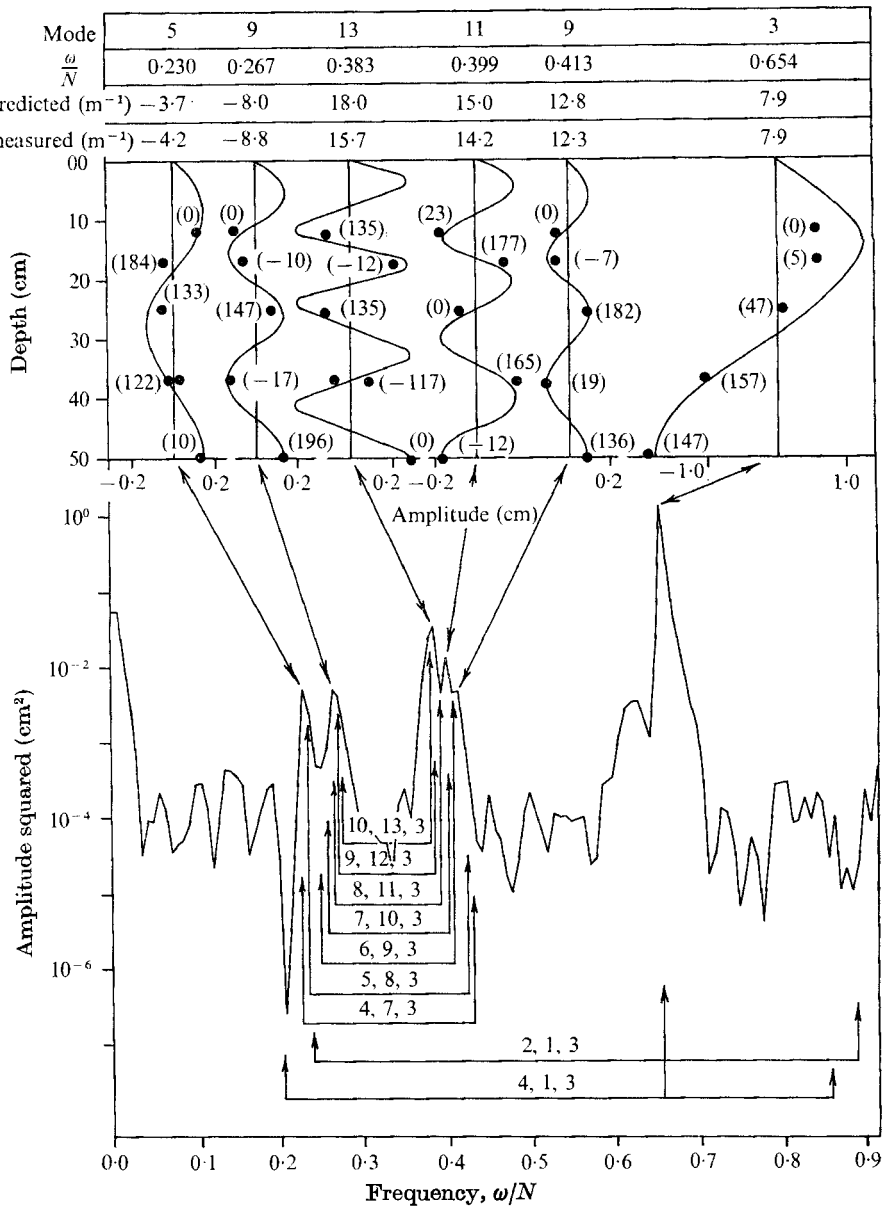

FIGURE 5. The periodogram, associated modal structure and comparison of the observed and predicted values of the horizontal wavenumbers for the large 3-wave alone experiment (3·47 m downstream, 50 cm depth, $\alpha = 9°$, $N = 0{\cdot}431$ sec^{-1}). In the upper part of the figure, the dark lines show the predicted modal structure; the solid circles, the observed wave amplitudes. The numbers in parentheses beside the solid circles give the observed values of the vertical phase differences. The arrows under the periodogram show the predicted location of some of the resonant triads associated with the 3-wave.

In the experiment, the observed 5-wave occurred at $\omega/N = 0{\cdot}230$, or within 1 % of the predicted value. The observed low frequency 5- and 9-waves, and the higher frequency 13-, 11- and 9-waves occur either at, or very close to, their predicted frequencies. We shall consider the accuracy of the agreement of the predicted and observed wave frequencies after discussing the second 3-wave experiment.

The second experiment, in which a small 1-wave at a frequency well off resonance is added to the 3-wave, shows, with the exception of the 13-wave, the same peaks observed in figure 5. In this experiment, the 1-wave had the properties

$$\omega_1/N = 0{\cdot}842, \quad \kappa_1 = 4{\cdot}7\,\mathrm{m}^{-1}, \quad \alpha = 1^\circ, \quad a_1 = 1{\cdot}1\,\mathrm{cm},$$

while the nearest (1, 3, 4) resonance requires

$$\omega_1/N = 0{\cdot}861, \quad \kappa_1 = 5{\cdot}8\,\mathrm{m}^{-1}.$$

Thus the triad is substantially detuned. Further, writing the amplitude a_1 in non-dimensional form, where $l_1 = \pi \times 10^{-2}$, gives

$$a_1 l_1 = 3 \times 10^{-2}, \quad a_1 \kappa_1 = 6 \times 10^{-2}.$$

Since the 1-wave is both detuned and of small amplitude, it should have little or no direct effect on the 3-wave.

For this experiment, figure 6 shows the periodogram, the associated modal structure and compares the observed and computed values of the horizontal wavenumbers. Under the periodogram, the arrows show the predicted location of the waves shown in figure 5. The main differences between figures 5 and 6 is that, in figure 6, the 13-wave cannot be discerned, and the peaks corresponding to the other modes are larger. For both experiments, table 1 lists the observed and predicted frequencies of the waves shown in figures 5 and 6. With the exception of the 11-wave in the 3-wave alone experiment, the observations lie within 1 % of the predicted values. There are two sources of error in table 1. First, the accuracy to which we can determine the observed wave frequency is primarily determined by the width of the frequency interval used in the Fourier transform program; in this case, we can determine ω/N to within $\pm 0{\cdot}002$. Second, the accuracy to which we can measure the density gradient determines the accuracy of the calculated triad positions. Comparison of the positions of resonant triads calculated from density profiles measured on two consecutive days yields an estimated accuracy for the calculated frequencies of $\pm 0{\cdot}002$. Thus, the maximum explainable error between the observed and calculated frequencies is about $\pm 0{\cdot}004$. Except for the 11-wave in the '3-wave alone' experiment, the observed and predicted frequencies agree to within $\pm 0{\cdot}005$.

To summarize, the combined results of the two experiments show that the large amplitude 3-wave spontaneously breaks down into components of the following sequence of triads that belong to set I: ($\underline{5}$, 8, 3), (6, $\underline{9}$, 3), (8, $\underline{11}$, 3), ($\underline{9}$, 12, 3) and (10, $\underline{13}$, 3), where we have underlined those waves observed in the experiments. We were unable to detect either the 7- or 10-wave of the (7, 10, 3) triad which would complete this ascending series. These waves belong to the set of triads with the largest computed growth rates.

The absence of triads with mode numbers greater than (10, 13, 3) is a real

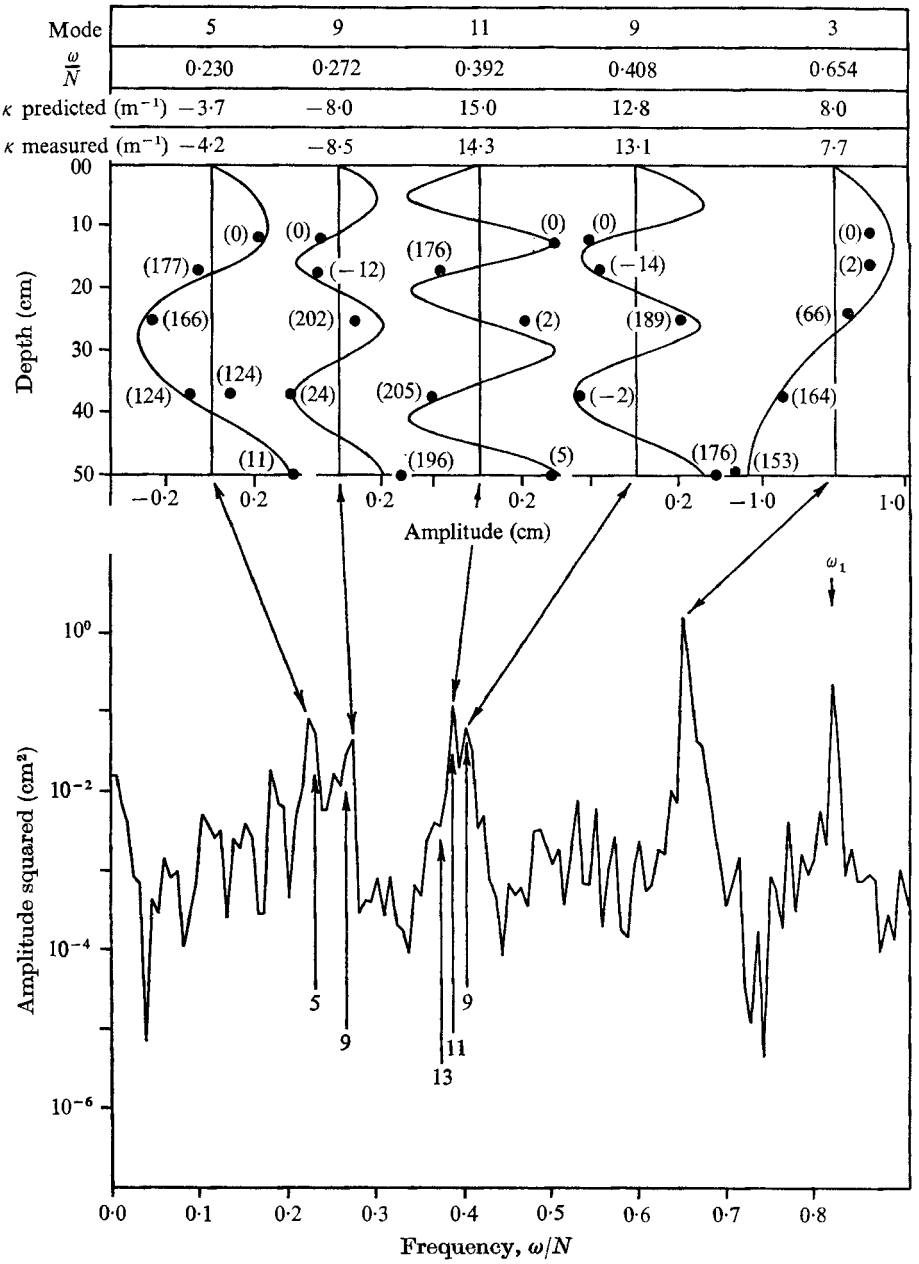

FIGURE 6. The periodogram, associated modal structure and comparison of the observed and predicted values of the horizontal wavenumbers for the large 3-wave plus small detuned 1-wave experiment (3·47 cm downstream, 50 cm depth, $\alpha = 1°$, $\alpha_3 = 9°$, $N = 0{\cdot}431\,\mathrm{sec}^{-1}$). The arrows under the periodogram show the predicted location of the waves observed in the 3-wave alone experiment.

Mode number	Frequency ω/N		
	3-wave alone	3-wave plus detuned 1-wave	Predicted
5	0·230	0·230	0·232
9	0·267	0·274	0·270
13	0·383	—	0·381
11	0·399	0·392	0·392
9	0·413	0·408	0·408

TABLE 1. Comparison of the observed wave frequencies for the two 3-wave experiments with the frequencies predicted from resonant triad theory.

feature of the experiments. With the present apparatus, waves with steepnesses similar to, but mode numbers higher than, those observed become more difficult to detect. Also, as § 3 shows, viscosity inhibits the unstable wave growth for mode numbers greater than 20. These effects, however, do not explain the sharp fall-off in energy above the frequencies corresponding to the 10-wave and below the frequency corresponding to the 13-wave on the periodograms shown in figures 4 and 5.

The question finally arises as to why we do not observe all of the members of the respective triads. There are two reasons for this. First, as figure 3 shows, the 8-wave, which could occur in two of the observed triads, is practically invisible to the present array. Second, for the sampling duration used, a small peak at one frequency could be hidden in the sidebands of a large peak at a nearby frequency. Presumably, the use of both a longer time series and more probes in the vertical would yield evidence of some of the missing modes.

4.3. *The unstable* 1*-wave*

Results of the experiments on 1-wave instabilities are consistent, but not as definitive as the results of the 3-wave experiments. Because we were unable to generate 1-waves of sufficient steepness as to be spontaneously unstable, the experiment which produced the clearest spectral peaks involved both the 1- and 3-waves generated at the paddle and tuned as follows:

$$\omega_1/N = 0{\cdot}868, \quad \kappa_1 = 5{\cdot}6\,\mathrm{m}^{-1}, \quad \alpha_1 = 2{\cdot}5, \quad a_1 = 3{\cdot}1\,\mathrm{cm},$$

$$\omega_3/N = 0{\cdot}673, \quad \kappa_3 = 8{\cdot}4\,\mathrm{m}^{-1}, \quad \alpha_3 = 6, \quad a_3 = 1{\cdot}3\,\mathrm{cm},$$

so that $a_1 l_1 \sim a_3 l_3 \sim 10^{-1}$, and $a_1 \kappa_1 \sim a_3 \kappa_3 \sim 10^{-1}$.

The wavenumber of the 4-wave at the difference frequency

$$\omega_4/N = 0{\cdot}195 \quad \text{is} \quad \kappa_4 = -2{\cdot}5\,\mathrm{m}^{-1},$$

which is within 11 % of $\kappa_1 - \kappa_3 = -2{\cdot}8\,\mathrm{m}^{-1}$. Because of the rapid variation of the wavenumber of the 1-wave with frequency at high frequencies, we found it difficult to tune this triad exactly.

Figure 7 shows the periodogram of the time series recorded at a distance of

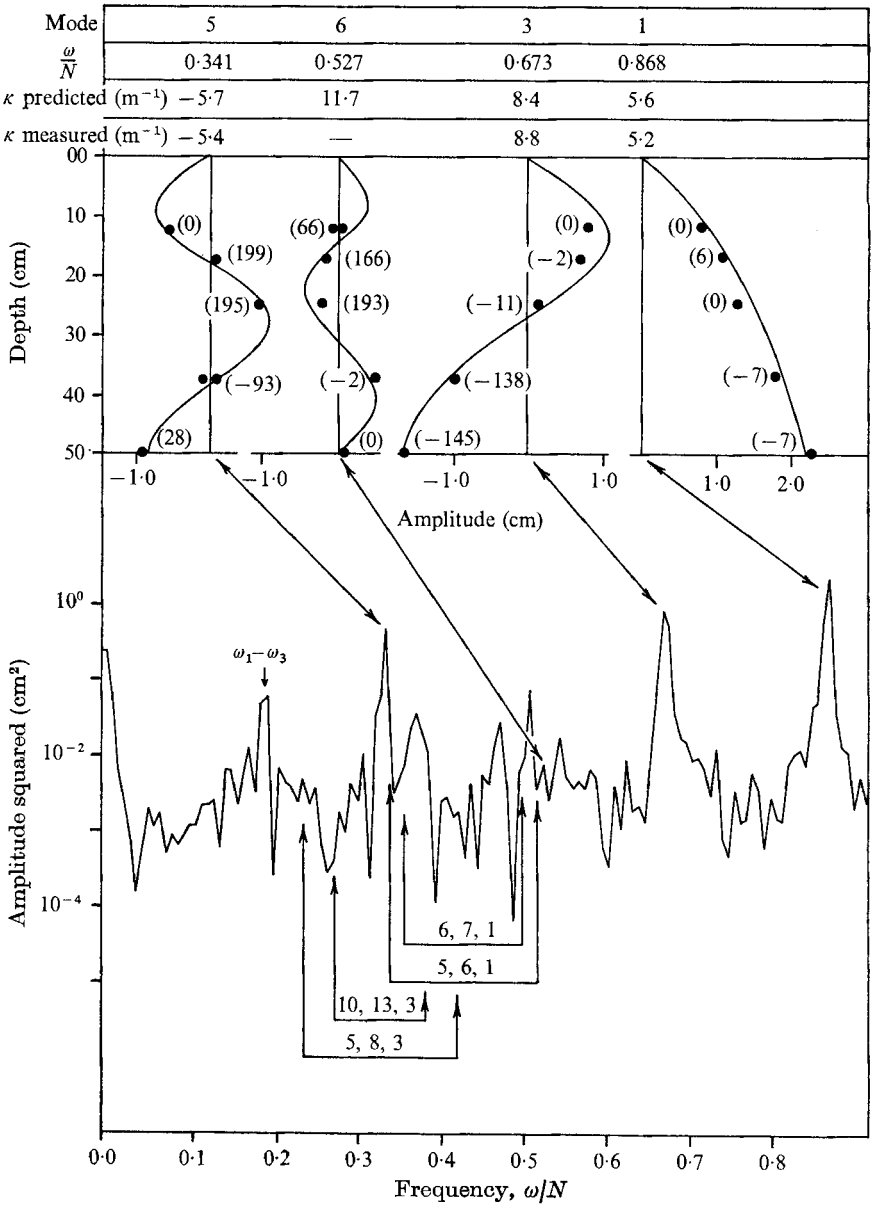

FIGURE 7. The periodogram, associated modal structure and comparison of the observed and predicted values of the horizontal wavenumbers for the large 1-wave plus small 3-wave experiment (3·47 m downstream, 50 cm depth, $\alpha_1 = 2{\cdot}5°$, $\alpha_3 = 6°$, $N = 0{\cdot}431\ \text{sec}^{-1}$).

3·46 m and at a depth of 50 cm, the modal structure associated with the best-defined peaks and compares the observed and calculated values of the horizontal wavenumbers. The clearest peaks, apart from the 1- and 3-waves, are the 5- and 6-waves, where the 6-wave has a node at a depth of 50 cm. The design of the array prohibited the measurement of the horizontal wavenumber of the 6-wave; however, the measured values of the other wavenumbers are close to their predicted values.

The arrows sketched in under the periodogram show some of the triads associated with the 1- and 3-waves. The observed 5- and 6-waves occur close to the predicted position of the (5, 6, 1) triad, which is a member of set I. The observed frequencies are $\omega_5/N = 0{\cdot}341$ and $\omega_6/N = 0{\cdot}527$, while the predicted values are $\omega_5/N = 0{\cdot}348$ and $\omega_6/N = 0{\cdot}520$. The error is greater than in the previous experiments, but the modal structure identification, particularly for the 5-wave, is very good. One possible reason for the increased error is that the 1-wave has a relatively high frequency ($\omega/N \simeq 0{\cdot}87$) and the dispersion relation program becomes less accurate at high frequencies. The periodogram also shows other peaks, both at frequencies slightly above the 5-wave frequency, and at frequencies slightly below the 6-wave frequency. Although the peaks were not sharp enough to permit us to identify their modal structure, they occur near frequencies corresponding to the positions of the ascending triads (6, 7, 1), (7, 8, 1), and so forth, which also belong to set I. Other arrows under the periodogram show the position of the (5, 8, 3) and (10, 13, 3) triads associated with the 3-wave. The peaks in these intervals are insignificant compared with those associated with the 1-wave, and thus we assume that the 3-wave is passive in this experiment.

The one unexplained feature of the present experiment is the relatively large peak at the difference frequency. If this peak were a 4-wave, it would have a minimum at a depth of 50 cm. A careful check of the calibration of the probe shows that its response is too nearly linear to have generated a spurious peak of this size; also, the peaks at the harmonics of ω_1 and ω_3 and at $\omega_1+\omega_3$ are much smaller than the peak at $\omega_1-\omega_3$. Possibly this peak could be caused by an as yet unidentified interaction among the other waves excited in the tank.

In summary, from the experiments on the 1-wave, we conclude that the 1-wave excites a set of triads from set I similar to those excited by the 3-wave, but, because the growth rates for the 1-wave instabilities are less than those for the 3-wave, we do not observe the set of triads with equal clarity.

4.4. *The multiple resonance*

We next discuss an experiment designed to study the (1, 3, 4, 7) multiple interaction. As § 3 shows, although an isolated multiple interaction is kinematically possible, a closed transfer of energy between the 1-, 3-, 4- and 7-waves is unlikely. Our experiments on the multiple interaction, which were run before the experiments on the 1- and 3-waves, showed energy transferred outside of the members of the multiple interaction to other spectral peaks, which could be understood only in the light of our study on the unstable 3- and 1-wave.

The experiment consisted of the following sequence. First, we generated a small amplitude 3-wave for a 30 min period, after which time we added a very small amplitude 1-wave to the 3-wave, and generated both waves simultaneously for another 30 min period. In both cases, 30 min was sufficient to yield a steady-state time series of 1024 points. We then stopped the paddle, recalibrated the probes, and repeated the above procedure for a 3-wave of moderate amplitude and the same 1-wave. We discovered that, as we increased the amplitude of the 3-wave, more energy was transferred outside of the (1, 3, 4, 7) to the 9-wave member of a (9, 12, 3) triad than was transferred to the 4- or 7-wave.

From the actual density gradient, the 1- and 3-waves had the following tuning:

$$\omega_1/N = 0{\cdot}889, \quad \kappa_1 = 5{\cdot}2\,\mathrm{m}^{-1},$$
$$\omega_3/N = 0{\cdot}667, \quad \kappa_3 = 8{\cdot}0\,\mathrm{m}^{-1},$$

so that $(\omega_1-\omega_3)/N = \omega_4/N = 0{\cdot}222$ and $\kappa_4 = -2{\cdot}8\,\mathrm{m}^{-1}$, where $\kappa_1-\kappa_3 = -2{\cdot}8\,\mathrm{m}^{-1}$; $(\omega_3-\omega_4)/N = \omega_7/N = 0{\cdot}444$, and $\kappa_7 = 11{\cdot}0\,\mathrm{m}^{-1}$, where $\kappa_3-\kappa_4 = 10{\cdot}8\,\mathrm{m}^{-1}$. As the above figures show, the waves were very closely tuned to the multiple interaction. For this tuning, we set the wave amplitudes as follows. In both cases,

$$\alpha_1 = 1°, \quad a_1 = 1{\cdot}2\,\mathrm{cm}, \quad a_1\kappa_1 \simeq 6\times10^{-2}, \quad a_1 l_1 \simeq 4\times10^{-2};$$

for the first (1, 3, 4, 7),

$$\alpha_3 = 6°, \quad a_3 = 1{\cdot}2\,\mathrm{cm}, \quad a_3\kappa_3 \simeq 1{\cdot}0\times10^{-1}, \quad a_3 l_3 \simeq 1{\cdot}1\times10^{-1};$$

and for the second,

$$\alpha_3 = 8°, \quad a_3 = 1{\cdot}6\,\mathrm{cm}, \quad a_3\kappa_3 = 1{\cdot}3\times10^{-1}, \quad a_3 l_3 \simeq 1{\cdot}5\times10^{-1}.$$

The experimental array consisted of 7 probes, positioned as follows: 1 probe at a distance of 2 m from the paddle and at a depth of 50 cm; 2 probes at 5 m and at depths of 37 and 50 cm; 1 probe at 7·5 m and at a depth of 37 cm; and 3 probes at 11 m and at depths of 37, 50 and 63 cm. The periodograms we shall discuss, with the exception of the paddle, are derived from time series recorded at the probe which is 7·5 m from the paddle, at a depth of 37 cm. This depth maximizes the amplitude of the 4-, 7- and 9-waves, while reducing the amplitudes of the 1-, and especially the 3-waves.

For the two 3-wave alone cases, figure 8 compares the periodogram of the paddle displacement for $\alpha_3 = 6°$ with the periodograms of the two 3-waves. The figure shows that as a_3 increases from 1·2 to 1·6 cm, new peaks occur in the frequency spectrum. The arrows over the periodogram show the predicted location of both the (1, 3, 4, 7) multiple resonance and the (9, 12, 3) triad. As might be expected from the study of the unstable 3-wave in § 4.2, the peaks on the periodogram of the larger 3-wave fall at those frequencies represented by the triads belonging to set I which lie between the (4, 7, 3) and (9, 12, 3) triads.

The periodogram also shows a small peak at ω_1. There is, however, doubt about the cause of this peak. An examination of a print-out of amplitude versus time shows that preceding this experiment there was some residual 1-wave propagating in the tank. At 18 min before the start of the time series from which we took our periodogram, the wave had (amplitude)$^2 = 2{\cdot}5\times10^{-3}\,\mathrm{cm}^2$. Since the size of the peak on the periodogram at ω_1 is $2{\cdot}4\times10^{-4}\,\mathrm{cm}^2$, this peak could have been caused by the residual 1-wave. On the other hand, for the (1, 3, 4, 7) tuning, the 3-wave could transfer energy to the 1-wave through the (4, 7, 3) triad. The periodogram of the 3-wave with $\alpha_3 = 6°$, which was the first experiment run that day, in fact shows a small peak at ω_1. Thus, the 1-wave on the upper periodogram is sustained at least in part by the (1, 3, 4, 7) tuning. Even though we cannot present unambiguous experimental evidence, we suspect that a single well-tuned 3-wave can excite all of the members of the multiple interaction.

The fundamental observation of this section remains that the addition of a

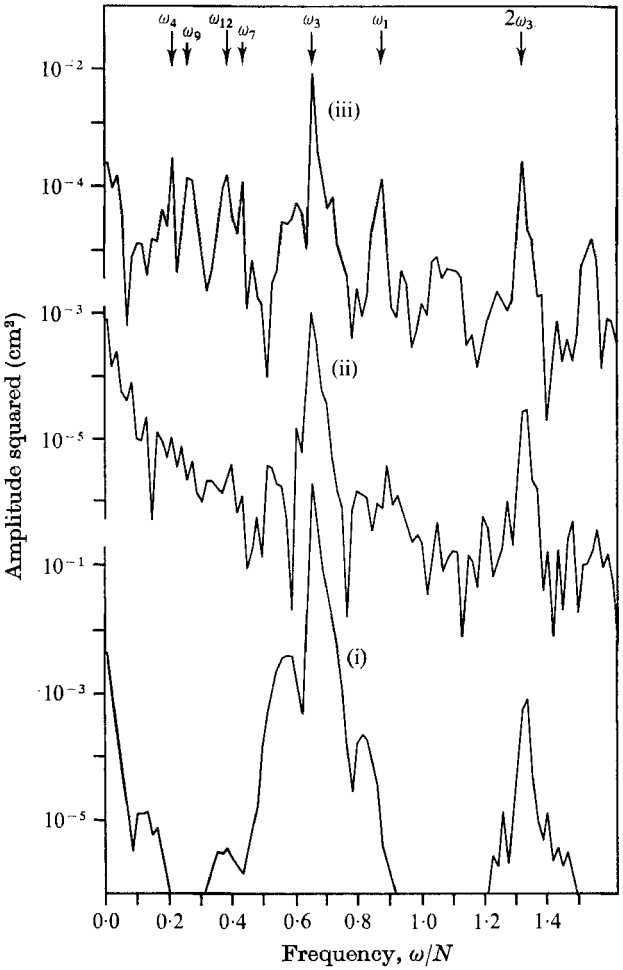

FIGURE 8. Comparison of the periodograms of (i) the paddle ($\alpha_3 = 6°$, $N = 0{\cdot}387\,\mathrm{sec}^{-1}$), (ii) the small 3-wave alone (7·5 m downstream, 37 cm depth, $\alpha_3 = 6°$), and (iii) the large 3-wave alone (7·5 m downstream, 37 cm depth, $\alpha_3 = 8°$) for the (1, 3, 4, 7) tuning.

small 1-wave to a large 3-wave at the (1, 3, 4, 7) resonant tuning results primarily in the transfer of energy to the 9-wave of the unstable (3, 9, 12) triad and, to a lesser extent, transfer to the ω_4 and ω_7 of the multiple interaction and ω_{12} of the unstable (3, 9, 12) triad. Our interpretation is that the very small 1-wave, itself stable on these time scales, acts mainly to enhance the noise level in the tank, and thereby catalyzes the 3-wave instability of the multiple tuning. Figure 9 illustrates the effect of adding a small amplitude 1-wave to the 3-wave with $\alpha_3 = 8°$. The upper and middle trace on figure 9 compare the periodogram of the 3-wave generated alone with that of the same 3-wave generated with a small 1-wave added at the (1, 3, 4, 7) tuning. These two periodograms are remarkably similar in appearance, except that, excluding the 3-wave itself, the peaks on the middle periodogram are two to three orders of magnitude larger than on the upper periodogram. In fact, because of the depth of the probe, the largest peak

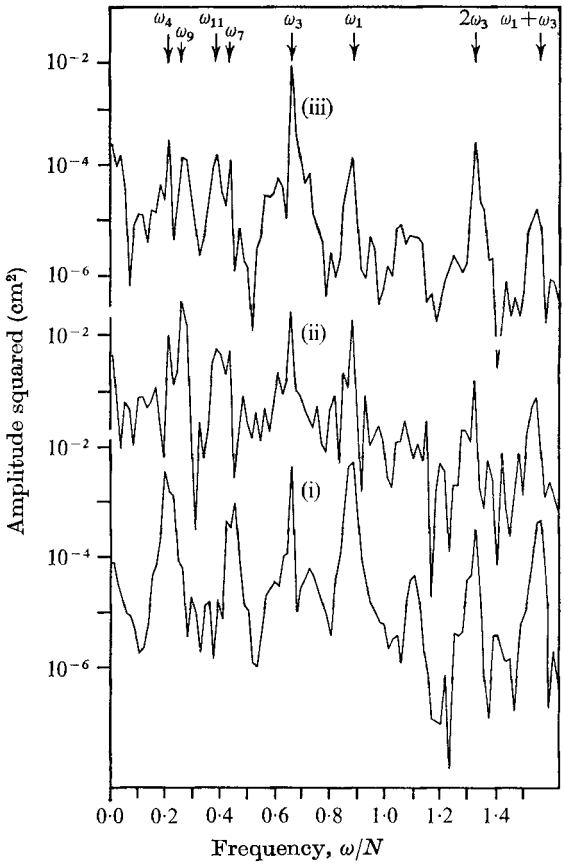

FIGURE 9. Comparison of the periodograms of (iii) the large 3-wave alone (7·5 m downstream, 37 cm depth, $\alpha_3 = 8°$), (ii) the large 3-wave plus the small 1-wave (7·5 m downstream, 35 cm depth, $\alpha_1 = 1°$, $\alpha_3 = 8°$), and (i) the small 3-wave plus small 1-wave for the (1, 3, 4, 7) multiple interaction (7·5 m downstream, 35 cm depth, $\alpha_1 = 1°$, $\alpha_3 = 6°$, $N = 0{\cdot}387\ \text{sec}^{-1}$). The arrows over the periodograms show the predicted location of the waves associated with the (1, 3, 4, 7) multiple interaction and the (9, 12, 3) triad.

on the middle periodogram occurs at ω_9. The enhancement of this 9-wave peak by nearly three orders of magnitude and the ω_4, ω_7, ω_9 and ω_{12} peaks by two orders of magnitude is a real effect of adding the 1-wave to the 3-wave at the multiple tuning.

The lower periodogram on figure 9 shows the case of the same small 1-wave added to a 3-wave of amplitude $\alpha_3 = 6°$. Comparison of this periodogram with the middle one shows that as we increase the 3-wave amplitude with the 1-wave amplitude held constant, the energy shifts from peaks at ω_4 and ω_7 toward peaks at ω_9 and ω_{12}. In figure 9, we also see that the peaks labelled ω_4 and ω_7 on the lower periodogram show a significant broadening compared to the middle trace. This is probably caused by the presence near ω_4 and ω_7 of other waves which are generated by the 3-wave instabilities.

Finally, figure 10 shows the amplitude of the 1-, 3- and 9-waves plotted versus distance for the (1, 3, 4, 7) ($a_3 = 1{\cdot}6$ cm) tuning. At a distance of 2 m from the

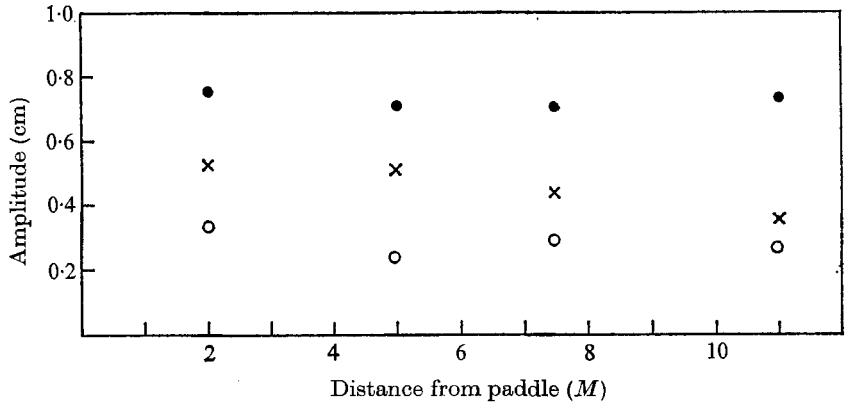

FIGURE 10. Amplitude versus distance for the (×) 1-, (●) 3-, and (○) 9-waves for the large 3-wave plus small 1-wave experiment: (1, 3, 4, 7) tuning, $\alpha_1 = 1°$, $\alpha_3 = 8°$.

paddle, the 9-wave takes on its maximum amplitude of 0·34 cm, and remains at a relatively large nearly constant amplitude at all of the downstream stations. There is no evidence of strong spatial variation; instead, the behaviour is consistent with the spatially uniform temporal instability described in § 3.

The question remains as to the exact cause of the selective amplification of the 9-wave. As shown in figure 9, the addition of the small 1-wave to the large 3-wave leads to a three order-of-magnitude growth of the 9-wave. We believe the small 1-wave plays the same role that the small detuned 1-wave played in the experiment described in § 4.2 and figure 6. There, the effect of the small detuned 1-wave was to enhance the peaks observed in the 3-wave alone case. The evidence of figure 9 supports that interpretation here.

5. Final remarks

We have discussed an experimental and theoretical study of the breakdown of progressive internal waves of modes 1 and 3 through resonant instabilities. The theoretical study predicts that a particular set of triads, which we call set I, have a larger growth rate than other possible resonant interactions. In our experiments, we observe as many as 5 members of the set I triads excited. The experimental section describes in detail the methods of modal identification. In less detail, we have also discussed the multiple interaction. For this case, the experiment showed, as the analysis suggested, that the instability of the multiple tuning is quite similar to the triad instabilities. The major importance of multiple tunings is that they may provide a way to transfer energy to frequencies above that of the generated unstable wave.

We thank Dr N. P. Fofonoff for his help and encouragement, and the staff of both the Woods Hole Oceanographic Institution and the Developmental Laboratory of the Department of Oceanography, University of Washington for their assistance. The computations were performed at the information processing centres of both the Woods Hole Oceanographic Institution and the

Massachusetts Institute of Technology. This work was supported by the Office of Naval Research under contracts 000-14-66-60-241, 3962(31) and 00014-67-A-0103-0014, and we thank them for their support. Contribution 628, Department of Oceanography, University of Washington, Seattle 98195; and contribution 2752 Woods Hole Oceanographic Institution, Woods Hole 02543.

Appendix A. The conductivity probe

The single-electrode conductivity probes used in these experiments follow a design suggested by Cacchionne (1970). They were constructed by drawing a tube of lead glass with an outer diameter of 0·32 cm into a capillary around a length of platinum wire with a diameter of 10^{-2} cm, as indicated in figure 11. The platinum wire was burned back into a sphere with a diameter of order 5×10^{-2} cm. The tube was then bent into an 'L', the end of the tube from which the wire emerged was packed with epoxy, and the sphere was coated with platinum black. For use in the tank, we soldered the lead of the probe onto the inner wire of a shielded cable, then fastened the probe with epoxy cement into the end of a long glass tube. To minimize the interference of the wave field with the wake of the support, the probe was placed in the tank with the horizontal arm oriented parallel to the wave crests. Experiments showed that the probes could detect displacements of order 5×10^{-2} cm.

Following a suggestion of G. Odell (private communication), the probes served as one arm of a constant-current a.c. Wheatstone bridge (figure 12). In a linearly stratified fluid, the voltage output of this particular circuit is almost exactly proportional to depth. From a circuit analysis of figure 12, the following equation relates the offset voltage E to the circuit parameters:

$$E_1 = ER_1\left[\frac{1}{R_2}-\frac{1}{R_p}\right]\left[1-\frac{R_1}{R_p}+\text{terms of order }\left(\frac{R_1}{R_3}\right)\right]. \tag{A 1}$$

From Gibson & Schwarz (1963), the resistivity of the single-electrode conductivity probe is

$$R_p = C/K, \tag{A 2}$$

where K is the conductivity measured in $\text{ohm}^{-1}\,\text{cm}^{-1}$, and C_1 is the cell constant of the electrode. For our probes, $C_1 \simeq 10\,\text{cm}^{-1}$. Over the range of salinity used in the experiments, the conductivity K is a linear function of s. From Chambers, Stokes & Stokes (1956), for a NaCl solution at 25 °C,

$$K = 2{\cdot}0 \times 10^{-3} + 1{\cdot}5 \times 10^{-3}s, \tag{A 3}$$

where s is the salinity in parts per thousand.

To relate the salinity to the density ρ, we use the empirical equation (Harned & Owen 1958)

$$\rho - \rho_0 = 7{\cdot}20 \times 10^{-4}s - 4{\cdot}84 - 10^{-6}s^{\frac{3}{2}}, \tag{A 4}$$

where ρ is measured in g cm^{-3} and ρ_0 is the density of pure water. If ρ increases linearly from 1·00 to 1·02 g cm^{-3} as the depth y, measured in cm from the free surface, increases from 0 to 100 cm, then (A 4) becomes

$$y = 3{\cdot}6s - 2{\cdot}42 \times 10^{-2}s^{\frac{3}{2}}. \tag{A 5}$$

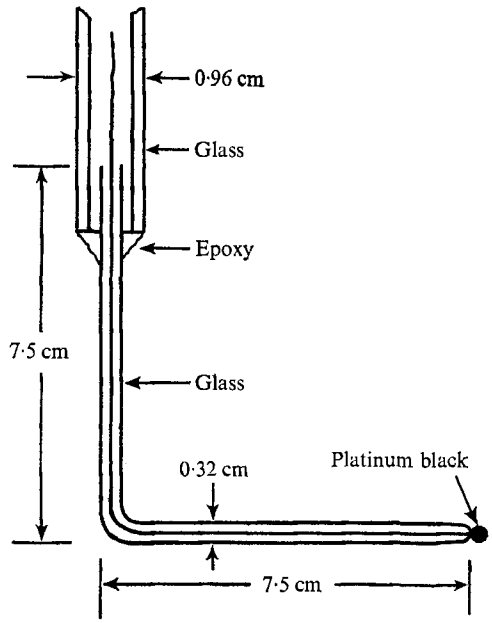

FIGURE 11. The conductivity probe.

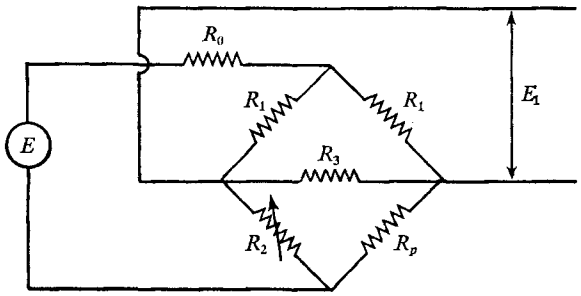

FIGURE 12. The constant-current a.c. bridge. $E = 0{\cdot}5$ volts, $60kh$, $R_0 = 0{\cdot}5$ ohms, $R_1 = 7$ ohms $R_3 = 10^5$ ohms, R_p is the probe impedance, and E_1 is the output voltage.

Expanding (A 5) in a power series about some y_0 and s_0, then solving for $s - s_0$ in terms of $y - y_0$ and setting $y_0 \simeq 3{\cdot}6 s_0$ gives

$$\frac{s}{s_0} - 1 = \left(\frac{y}{y_0} - 1\right)\left\{1 + 2{\cdot}5 \times 10^{-3} s_0^{\frac{1}{2}} \left(\frac{y}{y_0} - 1\right)\right\}. \tag{A 6}$$

From (A 6), the nonlinear dependence of s on y increases with depth.

To calculate the voltage response to changes in depth, we substitute (A 2), (A 3) and (A 4) into (A 1), and set $C = 10\,\mathrm{cm}^{-1}$, which gives

$$E_1 = EZ_1 1{\cdot}5 \times 10^{-4} s_0 \left(\frac{y}{y_0} - 1\right) \times \left\{1 + \left(\frac{y}{y_0} - 1\right)(2{\cdot}5 \times 10^{-3} s_0^{\frac{1}{2}} - 1{\cdot}5 \times 10^{-3} s_0)\right\}. \tag{A 7}$$

To determine the magnitude of the deviations from nonlinearity, we take a wave of amplitude 5 cm (which is larger than any wave used in the experiment) incident on a probe at a depth of 50 cm, which was, with one exception, the depth

of the deepest probe used in the experiment. Substitution of $y_0 = 50$ cm corresponding to $s_0 = 14‰$, and $y - y_0 = 5$ cm into (A 7), shows that the magnitude of the nonlinear term is order 0·1 %. Furthermore, if we fix the wave amplitude and decrease y_0, the magnitude of the nonlinear term decreases, so that, for the experiment, 0·1 % is the upper bound on the nonlinearities caused by the circuitry.

Appendix B. Derivations for constant N internal wave resonances

The experimental apparatus is modelled as a rectangular parallelepiped with rigid sides, top and bottom, having a wave generator at $x = 0$, and an absorber at $x = x_A$. The salt solution which fills the tank is taken as a non-diffusive incompressible Newtonian viscous fluid, which in its rest state is linearly stratified with $\rho = \rho_0(1 + N^2 y/g)$, where ρ_0 is the density at the free surface, y increases downwards from an origin at the free surface at rest, g is the acceleration of gravity, and $N^2 = (\partial\rho/\partial y)(g/\rho_0)$ is a constant. The following scheme for the non-dimensionalization of the governing equations suffices to demonstrate the resonant dynamic balances: horizontal and vertical length scales are k^{-1} and l^{-1}, respectively; the time scale is N^{-1}; the horizontal and vertical velocity scales are aNl/k and aN, respectively, where a is a typical vertical displacement; and the scale ρ' of density fluctuations due to wave motion is $a\partial\rho/\partial y$. The resulting non-dimensional forms of the incompressibility, continuity, and vorticity equations for inviscid two-dimensional motion are

$$\frac{\partial u}{\partial x} + \frac{\partial v}{\partial y} = 0, \tag{B 1}$$

$$\frac{\partial \rho'}{\partial t} - v = \epsilon\left(u\frac{\partial \rho'}{\partial x} + v\frac{\partial \rho'}{\partial y}\right), \tag{B 2}$$

$$\begin{aligned}\frac{\partial \rho'}{\partial x} + \frac{\partial}{\partial t}\left(\frac{\partial v}{\partial x} - \delta^2\frac{\partial u}{\partial y}\right) &= \sigma\frac{\partial}{\partial t}\left[y\left(\frac{\partial v}{\partial x} - \delta^2\frac{\partial u}{\partial y}\right) - \delta^2 u\right] + \epsilon\left[\delta^2\frac{\partial}{\partial y}\left(u\frac{\partial u}{\partial x} + v\frac{\partial u}{\partial y}\right) - \frac{\partial}{\partial x}\left(u\frac{\partial v}{\partial x} + v\frac{\partial v}{\partial y}\right)\right] \\ &\quad + O(\sigma\epsilon) + O(\sigma\epsilon^2),\end{aligned} \tag{B 3}$$

respectively, where u, v are horizontal and vertical velocity, $\rho + \rho'$ is the density in a state of motion, the parameter $\sigma = N^2/gl$, the aspect ratio $\delta = l/k$, and the steepness $\epsilon = al$. If we define a stream function ψ according to

$$u = -\partial\psi/\partial y, \quad v = \partial\psi/\partial x, \tag{B 4}$$

(B 1) is satisfied identically. Elimination of ρ' between the $O(1)$ parts of (B 2) and (B 3) then leads to the equation

$$\begin{aligned}\frac{\partial^2}{\partial t^2}\left(\frac{\partial^2}{\partial x^2} + \delta^2\frac{\partial^2}{\partial y^2}\right)\psi + \frac{\partial^2}{\partial x^2}\psi &= \epsilon\left\{\frac{\partial}{\partial t}\left[\delta^2\frac{\partial}{\partial y}(\psi_y\psi_{xy} - \psi_x\psi_{yy}) - \frac{\partial}{\partial x}(\psi_x\psi_{xy} - \psi_y\psi_{xx})\right]\right. \\ &\quad \left. - \frac{\partial}{\partial x}[\psi_y\rho'_x - \psi_x\rho'_y]\right\} - \sigma\left\{\frac{\partial^2}{\partial t^2}[\delta^2\psi_y + y(\psi_{xx} + \psi_{yy})]\right\} + O(\sigma\epsilon) + O(\sigma\epsilon^2).\end{aligned} \tag{B 5}$$

Neglect of terms of order ϵ, σ and their products yields the linear Boussinesq wave equation (in dimensional form)

$$\mathscr{L}(\psi) = \left[\frac{\partial^2}{\partial t^2}\left(\frac{\partial^2}{\partial x^2}+\frac{\partial^2}{\partial y^2}\right)+N^2\frac{\partial^2}{\partial x^2}\right]\psi = 0. \tag{B 6}$$

For constant N, (B 6) is satisfied by free wave solutions of the form

$$\psi = a\omega\cos(\kappa x-\omega t+\eta)\sin ly, \tag{B 7}$$

where η is a constant phase angle, ω is the frequency, and ω, κ, and l satisfy the dispersion relation

$$\frac{\omega^2}{N^2} = \frac{\kappa^2}{\kappa^2+l^2}, \tag{B 8}$$

(Phillips 1966). For our tank model, $l = n\pi/D$, where $n = 1, 2, 3, \ldots$ is the mode number of the wave(s), and D is the water depth.

The $O(\sigma)$ terms in (B 5), which are related to the Boussinesq approximation, account for the vertical variation in inertial mass caused by the stratification. Accounting for these terms, which may be done by using two-scale methods such as will be applied to the ϵ terms of (B 5) leads to an exponential multiplier in the amplitude of (B 7) with exponent proportional to $\sigma y/D$. This effect, similar to the one described by Lamb (1945, § 235), is small and will be ignored here. Similarly, the terms of $O(\sigma\epsilon)$ and $O(\sigma\epsilon^2)$ will be ignored.

The important balance is given by the terms of order ϵ. In anticipation of resonant interactions, we assume that the amplitudes and phase angles of the infinitesimal solution (B 7) are slowly varying functions of x, y, and t, by which is meant $\partial a/\partial t \sim aN\,O(\epsilon)$, $\partial a/\partial x \sim a\kappa\,O(\epsilon)$, etc., and similarly for η. Thus every differentiation generates a hierarchy of derivatives including an $O(1)$ term, a slowly varying $O(\epsilon)$ term, and a sequence of still higher order terms. Using operational rules such as

$$\left.\begin{aligned}\frac{\partial}{\partial t} &\to \frac{\partial}{\partial t}+\epsilon\frac{\partial}{\partial T}+\ldots,\\ \frac{\partial}{\partial x} &\to \frac{\partial}{\partial x}+\epsilon\frac{\partial}{\partial X}+\ldots,\\ \frac{\partial}{\partial y} &\to \frac{\partial}{\partial y}+\epsilon\frac{\partial}{\partial Y}+\ldots,\end{aligned}\right\} \tag{B 9}$$

where derivatives with respect to rapidly and slowly varying variables are denoted on the right by lower and upper case variables, respectively, and the x, t rapid variation is taken as $\exp i(\kappa x-\omega t)$, gives

$$\begin{aligned}\mathscr{L} \to\ & -\omega^2[\partial^2/\partial y^2+\kappa^2(N^2/\omega^2-1)]\\ & +\epsilon(2iN^2\kappa^2/\omega)\left[\frac{\partial}{\partial T}+\frac{\omega}{\kappa}\left(1-\frac{\omega^2}{N^2}\right)\frac{\partial}{\partial X}+i\frac{\omega}{\kappa^2}\frac{\omega^2}{N^2}\frac{\partial^2}{\partial y\,\partial Y}\right]+O(\epsilon^2).\end{aligned} \tag{B 10}$$

The $O(1)$ terms of $\mathscr{L}$ constitute the well-known eigenvalue problem for the modes and their dispersion relations. For constant N, (B 10) has constant coefficients and yields solutions of the form $\exp(ily)$. Direct substitution gives

$$(\kappa^2+l^2)N^2\left[\frac{\omega^2}{N^2}-\frac{\kappa^2}{\kappa^2+l^2}\right]\exp i(\kappa x+ly-\omega t) = 0. \tag{B 11}$$

If ω, κ, and l were replaced in the brackets above by $\omega+\Delta\omega$, $\kappa+\Delta\kappa$ and $l+\Delta l$, respectively, and terms were collected and grouped according to powers of the Δ terms, then the bracketed term would be regenerated by the lowest order group. By the very definition of partial differentiation, the next highest order grouping (first power of Δ) would have $\Delta\omega$ and $\Delta\kappa$ terms in the ratio of $(\partial\omega/\partial\kappa)_l$, and $\Delta\omega$ and Δl in the ratio of $(\partial\omega/\partial l)_\kappa$, where the derivatives are computed from the brackets in (B 11). Thinking, then, of $\epsilon\partial/\partial T$, $\epsilon\partial/\partial X$ and $\epsilon\partial/\partial Y$ of (B 9) as replacements for $\Delta\omega$, $\Delta\kappa$, and Δl in this argument, it is obvious that the $O(\epsilon)$ terms in the expansion (B 10) are of the form

$$\epsilon(2iN^2\kappa^2/\omega)\left[\frac{\partial}{\partial T}+C_{g_x}\frac{\partial}{\partial X}+C_{g_y}\frac{\partial}{\partial Y}\right],$$

where $C_{g_x}=(\partial\omega/\partial\kappa)_l$ and $C_{g_y}=(\partial\omega/\partial l)_\kappa$ are components of the group velocity. Alternatively, this form may be obtained by direct computation. Using this result with the traditional power-series representation

$$\psi=\sum_{r=0}^{\infty}\sum_{j=1}\epsilon^r\psi_j^{(r)},$$

$$\rho'=\sum_{r=0}^{\infty}\sum_{j=1}\epsilon^r\rho_j^{(r)},$$

but omitting the slow y variations, which are unnecessary here, (B 5), at $O(\epsilon)$, becomes (dimensionally)

$$\sum_j(2iN^2\kappa_j^2/\omega_j)\left[\frac{\partial}{\partial T}+(C_{g_x})_j\frac{\partial}{\partial X}\right]\psi_j^{(0)}+\mathscr{L}(\psi_j^{(1)})$$

$$=\sum_j\sum_m\frac{\partial}{\partial t}\{(\partial\psi_j^{(0)}/\partial y)\,\nabla^2(\partial\psi_m^{(0)}/\partial x)-(\partial\psi_j^{(0)}/\partial x)\,\nabla^2(\partial\psi_m^{(0)}/\partial y)\}$$

$$+(g/\rho_0)\frac{\partial}{\partial x}\{(\partial\rho_j^{(0)}/\partial y)\,(\partial\psi_m^{(0)}/\partial x)-(\partial\rho_j^{(0)}/\partial x)\,(\partial\psi_m^{(0)}/\partial y)\}. \quad \text{(B 12)}$$

To demonstrate a resonant instability, it is sufficient to take

$$\psi^{(0)}=\sum_{j=1}^{3}(a_{i,j}\omega_{i,j}/\kappa_{i,j})\cos(\kappa_{i,j}x-\omega_{i,j}t+\eta_{i,j})\sin l_{i,j}y,$$

and to expand ρ' in a similar form, where $(i,1)$, $(i,2)$ and $(i,3)$ are three integers to be specified. Determination of three suitable values of $\omega_{i,j}$ and $\kappa_{i,j}$ follows from the well-known kinematic conditions for resonance

$$\sum_{j=1}^{3}\omega_{i,j}=0,\quad\sum_{j=1}^{3}\kappa_{i,j}=0,\quad\sum_{j=1}^{3}l_{i,j}=0,\quad\omega_{i,j}^2/N^2=\kappa_{i,j}^2/(\kappa_{i,j}^2+l_{i,j}^2). \quad \text{(B 13)}$$

The existence of solutions to this set of algebraic equations is easily demonstrated by a graphical method described by Simmons (1969), together with the third relation of (B 13), that the sum of the mode numbers of such solutions vanishes. For convenience, then, the three integral values of i_j, $j=1,2,3$ will henceforth be taken equal to the absolute value of the mode numbers.

The nonlinear terms of (B 12) generate waves at every possible sum and difference frequency, wavenumber, and mode number. Those involving only sums

are balanced by the slowly varying part of (B 12), while all other sign combinations are balanced either by forced waves or bounded harmonics of $O(\epsilon)$, given by the $\rho^{(1)}$, $\psi^{(1)}$ solution in the traditional way (Lamb 1945). By collecting all the terms of (B 12) with similar rapidly varying parts (i.e. $\kappa_{i,j}x$, $\omega_{i,j}t$, $l_{i,j}y$), and balancing them individually, a process which is equivalent to averaging in the two-time sense, we obtain the interaction equations

$$\left.\begin{aligned} \frac{\partial}{\partial T}a_{i,j} + (C_{gx})_{i,j}\frac{\partial}{\partial X}a_{i,j} &= E_{i,j}a_{i,j+1}a_{i,j+2}\sin\eta, \\ a_{i,j}\left(\frac{\partial}{\partial T}\eta_{i,j} + (C_{gx})_{i,j}\frac{\partial}{\partial X}\eta_{i,j}\right) &= E_{i,j}a_{i,j+1}a_{i,j+2}\cos\eta, \end{aligned}\right\} \tag{B 14}$$

where (i,j) are the three mode numbers, j being interpreted modulo three, and $\eta = \sum_{j=1}^{3}\eta_{i,j}$. Simmons (1969) gives solutions for the variation of the phase angles $\eta_{i,j}$, but for our purposes it is sufficient to set $\eta = \frac{1}{2}\pi$, and $\eta_{i,j}$ = constant, so that

$$\frac{\partial}{\partial T}a_{i,j} + (C_{gx})_{i,j}\frac{\partial}{\partial X}a_{i,j} = E_{i,j}a_{i,j+1}a_{i,j+2}, \tag{B 15}$$

where, in dimensional terms,†

$$\begin{aligned} E_{i,j} = \frac{1}{8}\Bigg[&\frac{\omega_{i,1}\omega_{i,2}\omega_{i,3}}{N^2\kappa_{i,j}}\left(\frac{l_{i,j+1}}{\kappa_{i,j+1}} - \frac{l_{i,j+2}}{\kappa_{i,j+2}}\right)(\kappa_{i,j+1}^2 + l_{i,j+1}^2 - \kappa_{i,j+2}^2 - l_{i,j+2}^2) \\ &- \omega_{i,j+1}l_{i,j+1}\left(\frac{\kappa_{i,j+2}}{\kappa_{i,j+1}} - \frac{l_{i,j+2}}{l_{i,j+1}}\right) - \omega_{i,j+2}l_{i,j+2}\left(\frac{\kappa_{i,j+1}}{\kappa_{i,j+2}} - \frac{l_{i,j+1}}{l_{i,j+2}}\right)\Bigg]. \end{aligned} \tag{B 16}$$

The mean sum of kinetic and potential energy contained within a resonant triad is proportional to $\sum_{j=1}^{3}a_{i,j}^2$, therefore

$$\sum_{j=1}^{3}\left(\frac{\partial}{\partial T} + (C_{gx})_{i,j}\frac{\partial}{\partial X}\right)a_{i,j}^2 = a_{i,1}a_{i,2}a_{i,3}\sum_{j=1}^{3}E_{i,j}$$

must vanish by conservation of mean wave energy. It is a simple matter to show, from (B 13) and (B 16), that $\sum_{j=1}^{3}E_{i,j} = 0$, and also that $\sum_{j=1}^{3}\kappa_{i,j}E_{i,j}/\omega_{i,j} = 0$, so that the mean wave momentum is conserved.

REFERENCES

Cacchionne, D. A. 1970 Experimental study of internal gravity waves over a slope. Ph.D. thesis, Woods Hole Oceanographic Institution–MIT.

Chambers, J. F., Stokes, J. M. & Stokes, R. H. 1956 Conductances of concentrated aqueous sodium and potassium chloride solutions at 25°. *J. Phys. Chem.* **60**, 985.

Clark, C. B., Stockhausen, P. J. & Kennedy, J. F. 1967 A method of generating linear density profiles in laboratory tanks. *J. Geophys. Res.* **72**, 1393.

Davis, R. E. & Acrivos, A. 1967 The stability of oscillatory internal waves. *J. Fluid Mech.* **30**, 723.

† The signs in this form of the interaction coefficients are correct only if the wavenumbers and frequencies are defined so as to comply with (B 13).

GIBSON, C. H. & SCHWARZ, W. H. **1963** Detection of conductivity fluctuations in a turbulent flow field. *J. Fluid Mech.* **16**, 357

HARNED, H. S. & OWEN, B. B. 1958 *The Physical Chemistry of Electrolytic Solutions*, p. 358. New York: Reinhold.

HASSELMANN, K. 1967 A criterion for nonlinear wave stability. *J. Fluid Mech.* **30**, 737.

LAMB, H. 1945 *Hydrodynamics*. Dover.

MCEWAN, A. E. **1971** Resonant degeneration of standing internal gravity waves. *J. Fluid Mech.* **50**, 431.

MARTIN, S., SIMMONS, W. F. & WUNSCH, C. 1969 Resonant internal wave interactions. *Nature*, **224**, 1014.

PERKINS, H. 1970 Inertial oscillations in the Mediterranean. Ph.D. thesis, Woods Hole Oceanographic Institution–MIT.

PHILLIPS, O. M. 1966 *The Dynamics of the Upper Ocean*. Cambridge University Press.

SIMMONS, W. F. 1969 A variational method for weak resonant wave interactions. *Proc. Roy. Soc.* A **309**, 551.

THORPE, S. A. 1968 On the shape of progressive internal waves. *Phil. Trans.* A **263**, 563.

WUNSCH, C. I. **1969** Progressive internal waves on slopes. *J. Fluid Mech.* **35**, 131.